nature astronomy

Article

https://doi.org/10.1038/s41550-026-02790-0

Geology of Rimae Bode region as priority site candidate for China's first crewed lunar mission

Received: 21 May 2024

Accepted: 20 January 2026

Maosheng Yang [1], Jun Huang [1] ✉, Wajiha Iqbal [2], Lukas Wueller [2], Carolyn H. van der Bogert [2], Harald Hiesinger [2], Sascha Mikolajewski [2], Minggang Xie [3], Sen Hu [4] & Long Xiao [1,5]

Characterizing landing sites for future lunar crewed missions is key to maximizing the science output. Here we use orbital data to look at the equatorial Rimae Bode region, which is at the mare–highlands boundary and is a high-priority candidate for the upcoming Chinese crewed mission. We identify four distinct geological units: a dark mantle deposit; the Sinus Aestuum mare area; the Rimae Bode unit proper, formed by two distinct areas; and the highlands. The dark mantle deposit is pyroclastic material with relatively low albedo, whose thickness ranges from 77 m to 136 m. Sinus Aestuum is an ancient impact basin filled with low-Ti basaltic lavas with a maximum thickness of 193 m and with a 4-m-thick regolith mostly composed of local materials. Rima Bode I includes volcanic rilles that are potential sources for the basalts in Sinus Aestuum, as they share its spectral characteristics, whereas Rima Bode II exhibits high abundances of Th and Ti. Based on this information, we propose four prospective landing sites in the traversable areas, which provide a range of diverse geological samples, including volcanic debris, mare basalts, Copernicus crater ejecta and high-Th materials. Such a collection may provide insights into the geological evolution of the region and enhance our understanding of the lunar mantle composition and volcanic processes.

In 2023, China unveiled a crewed lunar programme, targeting its first Moon landing by 2030[1]. Candidate landing regions have been screened for scientific value and engineering feasibility. The initial 106 sites have been narrowed down to 14, among which Rimae Bode, a region located at the mare–highlands boundary of Sinus Aestuum and Mare Vaporum (Fig. 1a), ranked highly due to its diverse lithologies and favourable Earth-observation conditions[2]. Based on geomorphology and spectral characteristics, the Rimae Bode region can be broadly categorized into five geological units: the Sinus Aestuum unit, a highland unit, the Rima Bode I mare unit, the Rima Bode II mare unit and the dark mantle deposit (DMD) unit (Fig. 1b,c). This region has a complex geological evolution history from the Nectarian period to the Copernican period[3,4], and it hosts a diversity of materials, including high-Ti pyroclastic deposits in the DMD[5–7], low-Ti mare basalts[6,7], highland anorthosites[8], Copernicus crater ejecta[3], high-Th materials[9,10] and spinel-rich materials[10–12]. Notably, the DMD unit is characterized by low albedo and smooth surface[6,7,13], and the materials are of high scientific interest because they are explosively emplaced pyroclastics[14,15] and thought to originate from the deep

---

[1]State Key Laboratory of Geological Processes and Mineral Resources, Hubei Key Laboratory of Planetary Geology and Deep Space Exploration, School of Earth Sciences, China University of Geosciences, Wuhan, China. [2]Institut für Planetologie, Universität Münster, Münster, Germany. [3]College of Science, Guilin University of Technology, Guilin, China. [4]Institute of Geology and Geophysics, Chinese Academy of Sciences, Beijing, China. [5]State Key Laboratory of Lunar and Planetary Sciences, Macau University of Science and Technology, Macau, China. ✉e-mail: junhuang@cug.edu.cn

lunar interior[16]. In addition, Rimae Bode lies in an easily accessible, low-latitude, nearside location with generally flat, traversable terrain (Supplementary Fig. 1). Both the high scientific value and the favourable landing and exploration conditions make the Rimae Bode region a candidate for missions like the NASA Constellation programme[2,3,17–19] and China's first crewed lunar mission[2].

Here we focus on the area 8° N to 13° N and 1° W to 7° W (Fig. 1b) to address several scientific questions that remain unresolved for the Rimae Bode region: (1) the thickness and origin of pyroclastics in the DMD unit, (2) the composition and origin of the lunar soil in Sinus Aestuum, (3) the source of the basaltic magma in the Rima Bode I mare unit and (4) the stratigraphy and chronological relationships among the geological units. In addition, we propose four potential landing sites of high scientific interest to support future mission planning.

Results

DMD unit

In the study area, the DMD unit (red area in Fig. 1c) forms a smooth, low-albedo surface (Fig. 1b), and both the Arecibo S-band circular polarization ratio (CPR) (Fig. 2b) and rock abundance (Fig. 2c) within this unit are relatively low compared with the surrounding terrain. The DMD unit is of pyroclastic origin[6], characterized by elevated Ti and Fe (refs. 6,17) and water contents exceeding 300 ppm (refs. 4,20,21).

Using the spectral data recorded by the Moon Mineralogy Mapper (M^3) and the derived spectral parameters, regions of interest within each geological unit were identified and their mineralogical characteristics were analysed (Supplementary Fig. 2). The M^3 spectral data indicate that the DMD unit is characterized by low overall reflectance (Extended Data Fig. 1). After continuum removal, the spectra show a weak 1-μm absorption band but relatively high B1cen, B1asy and glass band depth values, consistent with glass and high-Ti material that shift the 1-μm band towards longer wavelengths[6,8]. The 2-μm absorption band is extremely weak and broad and lacking a distinct band centre, indicating that minerals with well-defined 2-μm absorption features (for example, pyroxene and spinel) do not dominate the M^3 spectra[22–24]. Previous studies identified two other large DMD units in Sinus Aestuum (5.7° N, 8.2° W and 5.5° N, 15.1° W) that exhibit a strong 2-μm absorption band, indicating possible enrichment in spinel or chromite[10–12]. Thus, independent constraints from impact-crater depths indicate that the pyroclastic deposits in the DMD unit reach thicknesses of ~77–136 m (Extended Data Fig. 2 and Supplementary Table 1; see the Supplementary Text for details).

Sinus Aestuum

Sinus Aestuum is situated ~400 km east of Copernicus crater and overlies a Nectarian-age impact basin that was subsequently buried by ejecta from Imbrium basin and infilled with mare basalts[12]. The terrain rises from lower elevations in the west to higher elevations in the east, with a pronounced step across the wrinkle ridges in Sinus Aestuum (Fig. 2a). Relatively high S-band CPR values (Fig. 2b) indicate that the mare surface is not mantled by fine-grained pyroclastic deposits[6]. The surface is relatively flat (average slope <8°) with a generally low rock abundance except near fresh craters and wrinkle ridges (Fig. 2c). TiO_2 abundances (4.7 wt%; Fig. 2d) confirm that the Sinus Aestuum basalts are low-Ti mare basalts[6].

The spectra of the Sinus Aestuum basalt exhibit distinct 1-μm and 2-μm absorption bands (Extended Data Fig. 1b). A band-parameter analysis yields a mean B1cen of 0.97 μm and B1asy values between −0.15 and 0.15, indicating that these basalts are essentially olivine-poor[23,25,26].

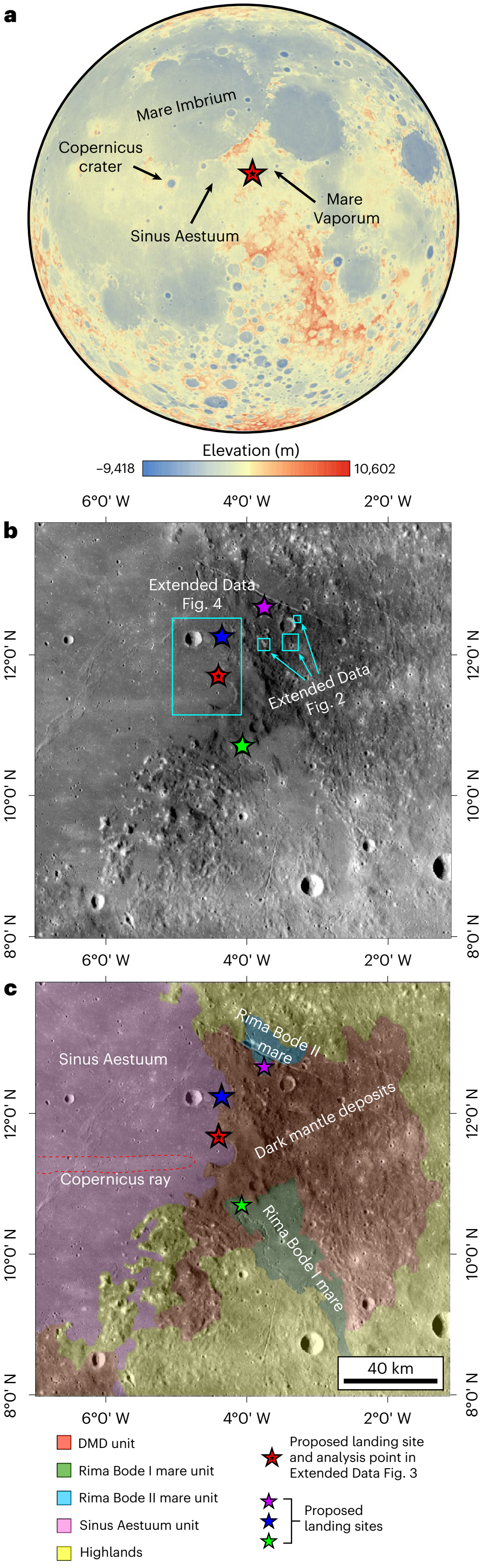

Fig. 1 | Rimae Bode region and proposed landing sites. **a**, Lunar nearside topography from the Chang'E-1 DEM[111] showing the location of the Rimae Bode region (red star) between Mare Imbrium, Sinus Aestuum and Mare Vaporum. **b**, Mosaic of the study area from images recorded by the wide-angle camera (WAC) of the Lunar Reconnaissance Orbiter camera (LROC). Proposed landing sites are shown as stars. Also shown are outlines of the regions in Extended Data Figs. 2 and 4. **c**, Simplified geologic map draped on the same base map, highlighting the Sinus Aestuum unit, Rima Bode I and II mare units, the DMD, highlands, the Copernicus ray and the proposed landing sites.

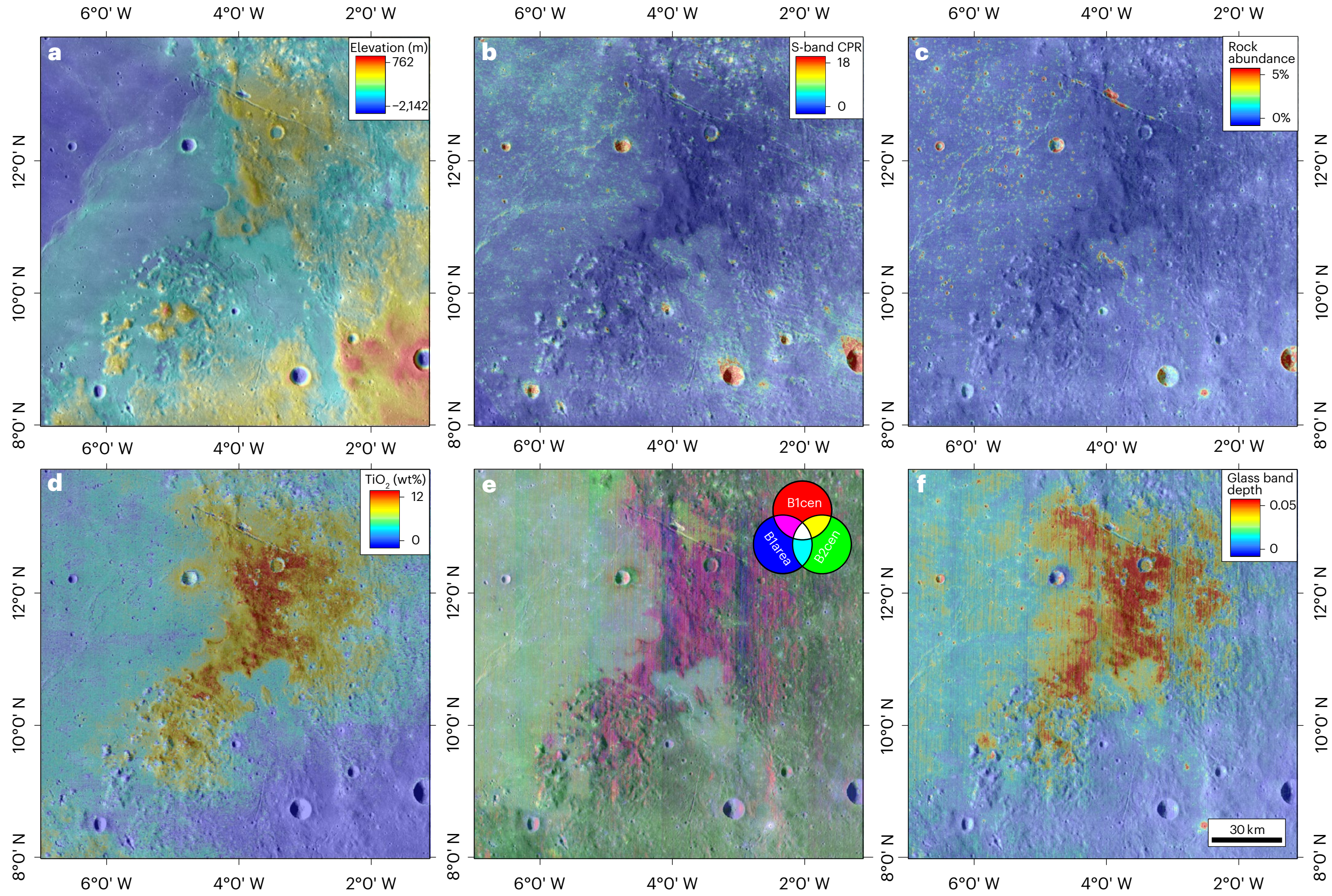

Fig. 2 | Remote-sensing datasets and derived products for the Rimae Bode region. a, SLDEM2015 topography[64]. **b**, Arecibo CPR map[70]. **c**, Lunar Reconnaissance Orbiter Diviner rock abundance[72]. **d**, TiO_2 abundance derived from WAC data[80]. **e**, RGB composite of band parameters derived from M^3, where R is the 1-µm band centre (B1cen), G is the 2-µm band centre (B2cen) and B is the 1-µm band area (B1area). **f**, Glass band depth derived from M^3.

The average B2cen of ~2.15 µm indicates that the spectra are dominated by pyroxene[22–24]. The near-infrared similarity between the Copernicus ray and the underlying Sinus Aestuum basalts indicates that Copernicus ejecta has not substantially altered the basaltic spectral characteristics, because the ray deposits are thin.

In eastern Sinus Aestuum, the regolith thickness ranges from 2 to 10 m, with a mean of ~4 m (Supplementary Fig. 3 and Supplementary Table 2). The regolith is dominated by local material, with ~10% exotic ejecta derived from Copernicus and Eratosthenes (Extended Data Fig. 3 and Extended Data Table 1). The underlying basaltic layer reaches a maximum thickness of 193 m (Extended Data Fig. 4 and Supplementary Table 1; see Supplementary Text for details).

Rima Bode I mare unit

The nomenclature used in this study is detailed in Supplementary Table 3. Rimae Bode is a network of rilles within the study area. Rima Bode I is the longest sinuous rille in the study region. It extends for ~115 km and trends predominantly NW–SE (Fig. 3a). Two other sinuous rilles in the area shown in Fig. 3a are not named on the Lunar Chart maps; we refer to them informally as Rima Bode III and Rima Bode IV (Fig. 3a). The Rima Bode I mare unit denotes the mare surface surrounding Rima Bode I. It is bounded by the DMD unit and adjacent highlands (Fig. 1c).

The basalts in Sinus Aestuum and the Rima Bode I mare unit have similar compositions and are both classified as low-Ti basalts[6,8]. The Sinus Aestuum and Rima Bode I basalts exhibit similar properties, including relatively high S-band CPR values and relatively low rock abundance and TiO_2 content, as well as comparable M^3 spectral characteristics (Fig. 2 and Extended Data Fig. 1).

We performed a detailed topographic analysis of the Rima Bode I rille floor, which revealed pronounced undulations along the profile (Fig. 3). From the elevation, rock abundance and morphological characteristics, we subdivided the rille into six segments (I_a to I_f). Segment I_a is contiguous with the Sinus Aestuum unit, and the closely matching spectra of the Sinus Aestuum basalts and the Rima Bode I mare unit (Fig. 2e) indicate a similar origin. Segment I_b lies at a higher elevation and has a maximum depth of ~80–100 m; abundant blocks along both channel margins (Fig. 4a) coincide with elevated rock abundances (Fig. 2c). Segments I_c and I_d show little variation in elevation. Segment I_c includes a possible degraded rille to the north, and a collapsed wall marks the western transition to segment I_d, whose levees are strongly degraded (Fig. 4b,c). Segment I_f extends into the highlands, where its elevation increases. Scarps at the distal end of Rima Bode I probably represent remnants of earlier basalt flows (Fig. 4c). Although no source vent has been identified near Rima Bode I, linear fissures associated with Rima Bode III and Rima Bode IV are visible (Fig. 4d,e) and may represent volcanic fissures.

Rima Bode II mare unit

Rima Bode II is a prominent lunar graben[27] that cuts both mare and highlands. The Rima Bode II mare unit (Fig. 1c) lies at a higher average elevation than Sinus Aestuum and is generally flat. S-band CPR values for the Rima Bode II mare unit fall between those of non-pyroclastic mare units and the DMD (Fig. 2b), consistent with partial mantling

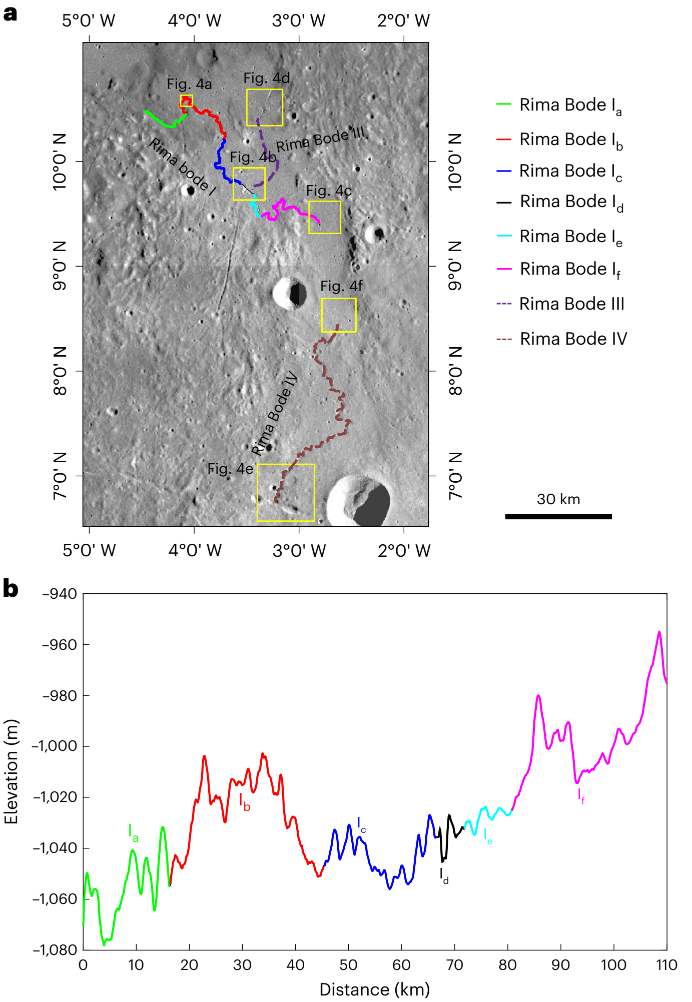

Fig. 3 | Sinuous rilles on the Rima Bode I mare unit. a, SELENE (Kaguya) terrain camera (TC) morning mosaic of the Rima Bode I mare unit showing three sinuous rilles: Rima Bode I (multicoloured solid line), Rima Bode III (purple dotted line) and Rima Bode IV (brown dotted line). Yellow boxes mark the areas shown in Fig. 4a–f. **b**, Longitudinal profile along the floor of Rima Bode I. Elevation data were smoothed with a moving-average filter, with a vertical accuracy of 3–4 m. Coloured segments correspond to the same colour-coded portions of the rille trace in **a**.

by pyroclastic deposits[6]. The TiO_2 abundance of the Rima Bode II basalts (7.5 wt%) is intermediate between those of the Sinus Aestuum basalts (4.7 wt%) and the DMD unit (9.6 wt%; Fig. 2d). Interestingly, thorium levels are elevated around the Rima Bode II mare unit[6,9]. Unlike the M^3 spectra of basalts in the other mare units, the Rima Bode II basalts exhibit a distinct 1-µm absorption and a broad 1.2–2.6-µm band, with an average glass band depth greater than 0.01 (Extended Data Fig. 1). These spectral characteristics are consistent with a mixture of pyroclastic deposits[6].

Discussion

Episodes of rille activity in the Rima Bode I mare unit

Rima Bode I comprises two rilles: a northern branch (segments I_a to I_c) and a southern branch (segments I_e and I_f). The two branches converge at the lowest part of the system, segment I_d, where the boundary is degraded and where Rima Bode III also intersects the rille (Fig. 4b). Abundant blocks occur along the walls of segments I_a to I_c (Fig. 4a), whereas few blocks are present along segments I_e and I_f. This contrast indicates that Rima Bode I records at least two distinct volcanic events. Crater densities differ at the confluence of Rima Bode I and Rima Bode III. The higher density in the south indicates an older surface, probably associated with Rima Bode III, whereas the lower density northern part records a younger lava flow (Fig. 4f). Additionally, the TiO_2 abundances decrease systematically from north to south. Because the northern part overlies an older, high-Ti DMD unit[5,28], this gradient is most probably due to different magmatic sources.

In contrast to previous interpretations, Rima Bode I is unlikely to be a single sinuous rille. Instead, it represents the confluence of two channels sourced from the north and south, each linked to a distinct volcanic episode. The observed morphology indicates the following sequence of volcanic activity within the Rima Bode I mare unit. First, Rima Bode III formed, with its distal reach flowing across an older Rima Bode I surface. This was followed by low-Ti basalt flooding that emplaced the present Rima Bode I mare. Finally, eruptions feeding the two branches of Rima Bode I and Rima Bode IV modified this surface, with all three rilles terminating at a common site.

Chronology of study area and the stratigraphy of eastern Sinus Aestuum

The chronological relationships of the geological units in our study area were determined based on the following criteria: (1) Pyroclastic distribution. Based on the areal extent of pyroclastic mantling seen in the radar data, we divided the units into two age groups: (1A) units pervasively covered by pyroclastic deposits (for example, DMD and Rima Bode II) were interpreted as predating the eruptions and (1B) units with little or no pyroclastic mantling (for example, the Sinus Aestuum unit and the Rima Bode I mare unit) were inferred to post-date these events. (2) Isotopic ages from returned samples. Copernican ejecta have been dated to 782 million years ago (Ma) based on $^{40}Ar/^{39}Ar$ analyses of Apollo 12 regolith[29]. Samples from Apollo 14 and Apollo 16 indicate that Imbrium basin formed 3.75–3.95 billion years ago (Ga)[30–34]. (3) The crater size–frequency distribution (CSFD). Copernicus yields an estimated age of 779–796 Ma (refs. 29,35,36). The age of the Sinus Aestuum unit is 2.96–3.70 Ga (ref. 28). The Rima Bode I mare unit (Supplementary Fig. 4) has an absolute model age (AMA) of $3.11^{+0.19}_{-0.34}$ Ga in the Eratosthenian. (4) Relative stratigraphic relationships[37]. Copernican ejecta overlie the Sinus Aestuum basalt unit, and Eratosthenian ejecta appear dimmer near the Copernican deposits, indicating that both craters post-date the Sinus Aestuum basalts. In addition, the rim of the Imbrium basin clearly overlaps that of the Sinus Aestuum basin, implying that Sinus Aestuum predates the Imbrium. The chronological relationships among the units are summarized in Table 1.

Furthermore, we constructed a geological column for eastern Sinus Aestuum (Extended Data Fig. 5), which comprises seven stratigraphic units.

The top layer is an ~4-m-thick layer of regolith (layer I), which is composed mainly of local materials derived from the underlying Eratosthenian low-Ti basalt with a minor admixture of exotic components sourced mainly from the Copernicus and Eratosthenes craters. Layer II comprises Eratosthenian low-Ti basalt dominated by pyroxene and feldspar, with an age of ~2.96 Ga (refs. 18,28). Similarities in spectral characteristics and AMAs indicate a common source region with the Rima Bode I unit. Within the Sinus Aestuum unit, impact craters that penetrate layer II excavate high-Ti material, implying a maximum thickness of ~193 m for this layer. Although this excavated material resembles the high-Ti pyroclastic deposits of the DMD unit, it may instead originate from stratigraphically earlier Eratosthenian (layer III) or later Imbrian (layer IV) high-Ti deposits. Layer V consists of volcanic pyroclastics emplaced by Late Imbrian explosive eruptions[38] and is ~77–136 m thick. These pyroclastic deposits are probably widespread at depth throughout the Sinus Aestuum basin[6]. Underlying layers VI and VII predate the pyroclastic eruptions. Layer VI consists of Early Imbrian basalt, whereas layer VII comprises ejecta from the Imbrium basin-forming impact. Using a ballistic sedimentation model[39], we estimated the Imbrium ejecta to be ~347 m thick in the Sinus Aestuum basin.

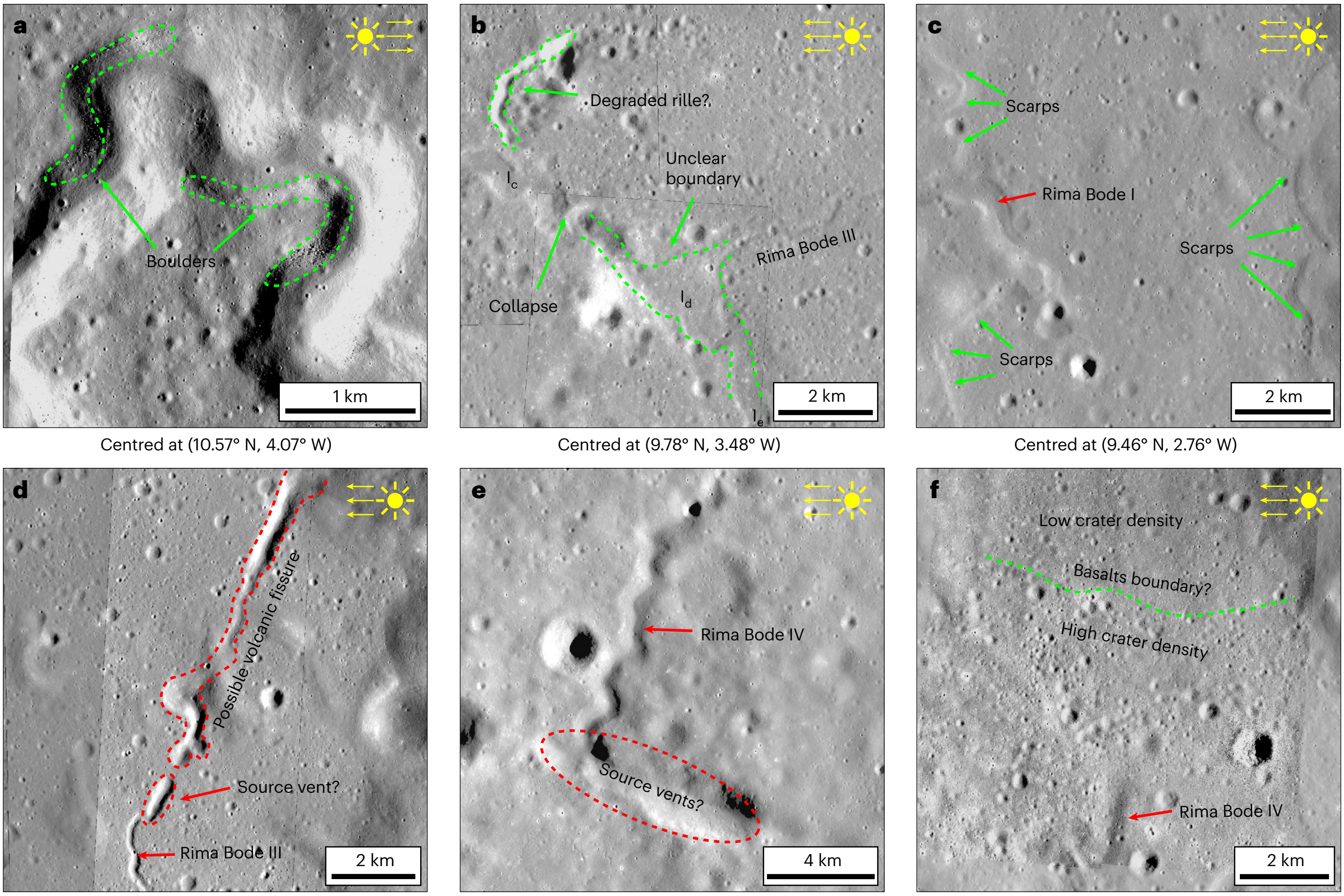

Centred at (10.57° N, 4.07° W)

Centred at (9.78° N, 3.48° W)

Centred at (9.46° N, 2.76° W)

Centred at (10.52° N, 3.33° W)

Centred at (6.84° N, 3.13° W)

Centred at (8.53° N, 2.62° W)

Fig. 4 | Various volcanic features related to the sinuous rilles. a–**f**, The base map combines several LROC narrow-angle camera (NAC) images (M1096522477R, M1108303722L, M1142468337L, M1142468337R, M1215450611L, M1215450611R, M1304822857R, M1394074753L and M1394074753R) with the Kaguya TC morning map. **a**, Distribution of boulders within Rima Bode I_b. **b**, Confluence of the northern branch (I_a to I_c) and southern branch (I_e to I_f) in Rima Bode I_d. **c**, Scarps near the eastern terminus of Rima Bode I (I_f) at the mare-unit boundary. **d**, Potential source vent of Rima Bode III and an adjacent possible volcanic fissure. **e**, Potential source vents of Rima Bode IV. **f**, Boundary between basalt units near the confluence with Rima Bode IV. Yellow arrows indicate the direction of solar illumination. Data from LROC QuickMap (https://lunar.quickmap.io).

Table 1 | Relative chronology of geologic units in the study area

Age[a]	Units	
	Volcanism	Impact
Copernican (800 Ma to now)		Copernicus ejecta ray
Eratosthenian (3.2–0.8 Ga)		Bode C[d]
	Rima Bode I mare (3.11 Ga)[d]	
	Sinus Aestuum basalt (2.96–3.70 Ga)[b]	Eratosthenes crater[a]
Imbrian (3.85–3.2 Ga)	Pyroclastic deposits (3.2–3.7 Ga)[c]	
Nectarian (more than 3.85 Ga)	Rima Bode II mare	Imbrium basin[a]
		Sinus Aestuum basin

[a]Ref. 110, [b]Ref. 18,28, [c]Ref. 38, [d]This study.

Rimae Bode as a priority landing site for China's first crewed lunar mission

The National Research Council has outlined key scientific objectives and the broader importance of lunar exploration[40]. We identify those goals that can be addressed in the Rimae Bode region (Extended Data Table 2). Owing to its abundant mare basalts, sinuous rilles and pyroclastic deposits, the Rimae Bode region is an exemplary site for investigating fundamental questions about lunar volcanism. In particular, collecting and returning pyroclastics from the DMD unit at Rimae Bode would greatly improve constraints on the composition of the deep lunar mantle, as demonstrated by the Apollo orange and green glass samples[15,41–44]. Indeed, the Rimae Bode region has already attracted considerable attention as a candidate landing site[3,6,13,17,45], including in studies associated with NASA's Constellation programme[19,46].

The Rimae Bode region also satisfies key engineering constraints. It meets stringent requirements on terrain[47], thermal environment, illumination and radiation, which are aimed at ensuring landing safety, robust communications, sufficient power supply and effective support for astronauts' surface operations. The scientific goals and engineering constraints are summarized in Extended Data Table 3.

Feasible landing sites and possible samples to be returned

We used extravehicular activity (EVA) traverses from the six Apollo landing missions to constrain the maximum radius for science target searches and astronaut mobility[48]. Apollo 11, Apollo 12 and Apollo 14 astronauts conducted walking EVAs, with maximum traverse distances <2 km (refs. 49–51). Apollo 15, Apollo 16 and Apollo 17 employed lunar roving vehicles, which enabled substantially longer traverses[52–54]. Given

https://doi.org/10.1038/s41550-026-02790-0

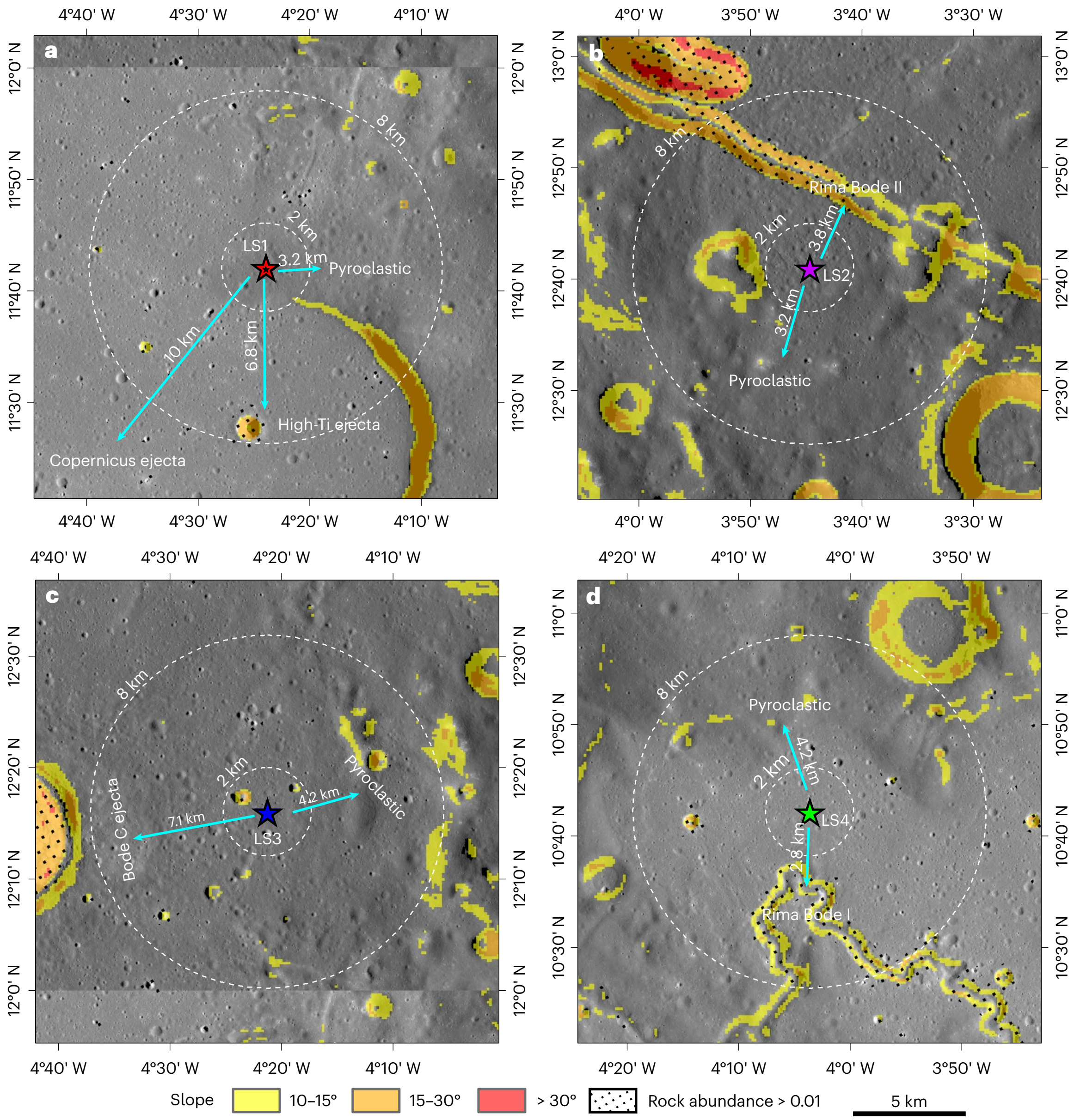

Fig. 5 | Four feasible landing sites, high-value science targets and surface hazards. **a**–**d**, Stars (red, purple, blue and green) mark the proposed landing sites: LS1 (**a**), LS2 (**b**), LS3 (**c**) and LS4 (**d**). The red star indicates a location that could be used to analyse the abundance of exotic ejecta on the eastern side of Sinus Aestuum (Extended Data Fig. 3). Arrows highlight high-value scientific targets. Areas with slopes >10° or rock abundance >0.01 are treated as presenting elevated safety risks. The base map combines the TC morning map and evening map.

that the longest single-traverse distance during Apollo 17 was 8.2 km (refs. 54–56), we restricted candidate science targets to within 8 km of the proposed landing site. From the topography, slope, rock abundance and spectral properties, we identified four feasible landing sites: in the Rima Bode I mare, Rima Bode II mare and Bode C and on the wall of the large crater (Fig. 1b,c). Details of these candidate sites are summarized in Extended Data Table 4.

Landing site 1 (Fig. 5a) lies north of a large crater wall at the boundary between Sinus Aestuum and the DMD unit. This site would allow the collection of the Sinus Aestuum low-Ti basalts and the surface regolith. The CSFD analysis yielded an AMA for Sinus Aestuum of 2.97–3.70 Ga, indicating that these basalts are Upper Imbrian to Eratosthenian[28]. The crater wall exposes the stratigraphic relationships among the geologic units at the landing site. East of the wall lies the DMD unit, where overlying pyroclastic deposits can be sampled for studies of lunar volcanism. Additionally, the relatively high-albedo Copernicus ray lies ~10 km south-west of the landing site, although beyond the 8-km radius. Regolith within this range is expected to contain Copernicus ejecta.

Landing site 2 (Fig. 5b) lies south of the Rima Bode II mare unit on high-Th basalt adjacent to Rima Bode II. High-Th regions within the Procellarum KREEP Terrane are confined around the Imbrium basin, supporting the hypothesis that most lunar surface Th derives from the Imbrium impact event[57]. The proximity of the Rima Bode II mare unit to the Imbrium basin would enable sampling of high-Th materials to investigate the origin of lunar Th and its connection to the Imbrium impact. Approximately 3.2 km south of the landing site lies the edge of the DMD unit, where pyroclastic deposits could be sampled, and at ~3.8 km to the north, the Rima Bode II graben provides access to characteristic lunar volcanic morphologies.

Landing site 3 (Fig. 5c) is ~6 km east of the Bode C crater. In addition to enabling sampling of local Sinus Aestuum basalts and pyroclastics from the DMD unit ~4.2 km to the east, the site is also close to the high-albedo ejecta on the eastern side of Bode C. Subsurface materials excavated by Bode C, together with high-Ti deposits analogous to those of the DMD unit, may be present and would provide important constraints on the geological evolution of Sinus Aestuum.

Landing site 4 (Fig. 5d) lies north-west of the Rima Bode I basalt unit on low-Ti Eratosthenian basalt, with the DMD unit to the north. Approximately 2.8 km south of the site lies the Rima Bode I_b segment (Fig. 3), a possible source of the Rima Bode I rille; samples from this area could provide key constraints on the volcanic history of the Rima Bode I unit.

Astronaut safety is the primary constraint on EVA planning, which requires that traverses avoid steep slopes and large elevation changes. During Apollo, astronauts climbed up to ~150 m and traversed slopes as steep as 15°, but such terrain was physically demanding[56]. Therefore, EVA routes should remain mainly on gentle slopes to minimize the time on steep ground. Boulder distributions must also be considered. Although boulders complicate safe landing and traverse planning, they offer convenient access to large rock samples. Using slope and rock-abundance data, we completed a first-order safety assessment around our proposed landing sites (Fig. 5). For future crewed missions, detailed geological surveys—including high-resolution digital elevation models (DEMs) and rock-abundance maps—will be essential for reducing the risk and optimizing the scientific return.

Crewed lunar missions have a key advantage over robotic exploration: astronauts can deploy complex scientific instruments on the surface. During the six Apollo missions, a diverse suite of experiments was emplaced, yielding data that transformed our understanding of lunar geology and geophysics[58,59]. A new crewed mission, more than 50 years later, would offer the opportunity to deploy similar or entirely new instruments, thus providing fresh constraints on lunar processes. EVA planning must also consider the science package, including instrument types, deployment time and optimal placement sites.

As a high-priority landing area for China's first crewed mission, the Rimae Bode region promises to provide opportunities for rich scientific exploration and notable discoveries in lunar geology. The strategic integration of geological and spectral analyses has painted a comprehensive picture of the potential of the region.

Methods

Chang'E-1 global DEM

The laser altimeter onboard the Chang'E-1 mission measured the lunar surface elevation. We used the DEM[60] generated from the laser altimetry data to analyse the overall topography of the study area (Fig. 1a).

LRO WAC and NAC images

LROC is a system of three cameras: two NACs operating at ~50 cm px^{-1} and a WAC recording in seven bands at 100 m px^{-1} (ref. 61). We used the LROC WAC Global Morphology Mosaic[62] to study the regional geologic context and the NAC images in detailed geomorphological investigations.

SELENE TC and SLDEM2015

The TC onboard the Selenological and Engineering Explorer (SELENE) is a stereo camera imaging the lunar surface at a spatial resolution of 10 m. The SELENE team released morning and evening maps with near-global coverage based on the TC data[63]. In addition, a higher-resolution DEM, known as SLDEM2015[64], was produced with the TC and lunar orbiter laser altimeter data. SLDEM2015 covers latitudes of ±60° with a horizontal resolution of ~59 m px^{-1} and a vertical accuracy of ~3 m to 4 m (ref. 64). We used SLDEM2015 for the detailed topographic analysis (Figs. 2a, 3b and 5).

Arecibo S-band CPR maps

Based on samples and images from the Apollo 17 mission, the surface of lunar pyroclastics in DMDs appears smooth[65–67], rendering it sensitive to radar-based studies (for example, Arecibo and the miniature radio-frequency instrument onboard the Lunar Reconnaissance Orbiter) of pyroclastic-rich units[6,68,69]. An area that is heavily covered with pyroclastics appears smooth and dark in albedo images and has lower radar returns than surrounding units not covered with pyroclastics[6].

Arecibo S-Band CPR maps were generated using a 12.6-cm (S-band) circularly polarized signal transmitted from the Arecibo Observatory. These maps were produced by averaging pixel values within a 5 × 5 moving window and then calculating the ratio of the averaged same-circular-polarization data to the averaged opposite-circular-polarization data[70]. We used the CPR map to identify the distribution and relative thickness of pyroclastics in the study area[6] (Fig. 2b).

Diviner rock abundance

The Diviner Lunar Radiometer Experiment on the Lunar Reconnaissance Orbiter is investigating the thermal environment of the lunar surface[71]. Extensive research based on Diviner datasets has produced maps of surface temperature, thermophysical properties and rock abundance[72–78]. Recently, Powell et al.[75,79] produced an updated lunar rock-abundance map using ~13 years of Diviner observations. Compared with earlier thermophysical products, this rock-abundance map incorporates a larger dataset with a higher spatial resolution, corrections for Diviner instrument errors and an improved thermal model. We used this rock-abundance map to characterize the surface environment of our study area (Fig. 2c).

WAC TiO_2 abundance

TiO_2 abundance (wt%) was estimated from the LROC WAC 321/415 nm band ratio over 70° N to 70° S (ref. 80). The TiO_2 map was derived from the WAC Hapke-normalized mosaic constructed from ~124,300 WAC images acquired between 21 January 2010 and 1 May 2013. The TiO_2 wt% was obtained by linearly correlating the TiO_2 contents of returned lunar soil samples with the WAC 321/415 nm ratios at the sampling sites and then applying this relationship to the global 321/415 nm ratio mosaic to generate a TiO_2 abundance map[80–82]. Using this WAC TiO_2 dataset, we measured the average TiO_2 content of each geologic unit (Fig. 2d).

Moon Mineralogy Mapper

The M^3 on Chandrayaan-1 was a high-precision imaging spectrometer with 140 m px^{-1} spatial resolution and 86 spectral bands spanning 430–3,000 nm (ref. 83). Its level 2 reflectance data, obtained from the NASA Planetary Data System, have been corrected using radiometric[84], geometric[85], thermal[86], photometric[87,88] and ground truth data[89]. Owing to large temperature variations during M^3 observations, the data are divided into cold (OP1B and OP2A) and warm periods[90]. To minimize the effects of these thermal variations on the spectral data, we used the OP1B M^3 data in the spectral analysis to identify mineral compositions (M3G20090205T211213, M3G20090205T225833, M3G20090206T010833, M3G20090206T030351, M3G20090206T050647 and M3G20090206T065053).

Spectral data processing and band parameters

Following Horgan et al.[91], we calculated the band parameters to quantitatively characterize the spectral features. The parameters include the 1-µm band centre (B1cen), 1-µm band asymmetry (B1asy), 2-µm band centre (B2cen) and glass band depth. A fourth-order polynomial was fitted to the continuum-removed M3 spectra in the vicinity of the 1-µm and 2-µm bands, and the wavelengths of the minima of these fits were taken as B1cen and B2cen, respectively[91]. The 1-µm band asymmetry (B1asy) was defined as the difference between the integrated areas on the short- and long-wavelength sides of B1cen, where the area was computed by summing $(1 - R_c)\Delta\lambda$ over all channels (R_c is the continuum-removed reflectance and $\Delta\lambda$ is the spectral sampling interval)[91]. These three parameters together are effective for distinguishing most Fe-bearing minerals[91]. The glass band depth was calculated as 1 minus the mean continuum-removed reflectance at 1.15 μm, 1.18 μm and 1.20 μm, and we used it as a proxy for the relative abundance of glass[91,92]. Our spectral analysis followed three steps: (1) generating continuum-removed spectra from M^3 level 2B data, (2) calculating the band parameters from the continuum-removed spectra and (3) comparing the spectra using two-parameter band–band plots.

Crater-based estimation of unit thickness

To estimate the thicknesses of the geological units, we used the crater floor depths as constraints. For each crater, we extracted topographic profiles along four azimuths (N–S, E–W, NE–SW and NW–SE) and measured the elevation difference between the crater floor and the surrounding relatively flat terrain (Extended Data Fig. 2c,f). We then calculated the mean and standard deviation of the four measurements. These depths were interpreted as upper bounds on the thickness of the Sinus Aestuum mare basalts and the DMD pyroclastic deposits (Supplementary Table 1).

Regolith thickness from concentric craters

Following Quaide and Oberbeck[93], we estimated the lunar regolith thickness using relatively fresh concentric craters with diameters <250 m. For such craters, the regolith thickness T is given by

$$T = \left(k - \frac{D_F}{D_A}\right) D_A \tan(\alpha)/2,$$

where D_A is the diameter of the outer concentric ring, D_F is the diameter of the inner concentric ring, k is an empirical constant (0.86) and α is the angle of repose of lunar regolith (31°)[93]. We identified concentric craters in LROC NAC images acquired at incidence angles <55°, which provided favourable illumination for recognizing concentric structures[94]. Only relatively well-preserved craters with diameters <250 m were used to estimate the regolith thickness[93,95].

Modelling exotic ejecta in the regolith of eastern Sinus Aestuum

Lunar regolith typically consists of locally derived material mixed with ejecta from distant impact craters ('exotic' material). Constraining the composition and origin of this exotic component is important for future laboratory traceability studies. To quantify the influence of exotic crater ejecta on the eastern Sinus Aestuum region, we employed the ballistic sedimentation model[39] to calculate the thickness and abundance of exotic ejecta. The analysis proceeded in four steps: (1) computing the thickness of ejecta reaching eastern Sinus Aestuum and identifying the main source craters used in the vertical-mixing model, (2) estimating the size–frequency distribution of secondary craters formed by the impact of this ejecta, (3) calculating the volume and mass of local material excavated by exotic ejecta and (4) uniformly mixing the exotic ejecta with the excavated local materials to evaluate how the relative abundances of exotic and local components vary with depth below the surface[39,96]. The relative chronology of the exotic ejecta is constrained by CSFD and isotopic data[29,35,36,96,97].

CSFD dating of the Rima Bode I basalts unit

The AMA of the Rima Bode I basalt unit was determined using the CSFD[98–101]. We used OpenCraterTool[102] to count craters with diameters >200 m on the Kaguya TC morning mosaic within the Rima Bode I basalt unit. To minimize contamination by secondary craters, we identified and excluded obvious chains and clusters based on their morphologies[103].

AMAs were then derived with Craterstats2[104] using the chronology and production functions of ref. 105 and the Poisson probability analysis of ref. 106. To assess the influence of less obvious secondaries, we applied the randomness analysis of ref. 107, which detects statistically significant crater clustering that may not be apparent by eye. The counting area and detailed CSFD results for the Rima Bode I basalt unit are shown in Supplementary Fig. 4.

Data availability

The Chang'E-1 global DEM is provided by the China National Space Administration and the Science and Application Center for Moon and Deep Space Exploration and is available from https://moon.bao.ac.cn/ with a registered account. LROC WAC Global Morphology Mosaic data are available from https://astrogeology.usgs.gov/search/map/moon_lro_lroc_wac_global_morphology_mosaic_100m (ref. 62). LROC NAC images can be obtained from https://data.lroc.im-ldi.com/lroc/search with IDs. SELENE (Kaguya) TC morning mosaics are available at https://darts.isas.jaxa.jp/planet/pdap/selene/product_search.html, and SLDEM2015 can be accessed from https://darts.isas.jaxa.jp/app/pdap/selene/. M^3 reflectance data are available from https://pds-imaging.jpl.nasa.gov/volumes/m3.html ref. 108. WAC TiO_2 abundance maps can be accessed from https://wms.lroc.asu.edu/lroc/view_rdr/WAC_TIO2. Diviner rock-abundance data are available at https://doi.org/10.25346/S6/LFAVXU (ref. 79). Arecibo S-band CPR maps can be obtained from https://pds-geosciences.wustl.edu/lunar/arcb_nrao-l-rtls_gbt-5-12.6cm-v1/slrm_90xx/data/. The spectral parameter mosaics and cross-sectional profile data generated in this study are available via Zenodo at http://zenodo.org/records/17767133 (ref. 109).

References

1. China's crewed lunar mission fully initiated (我国载人登月任务全面启动). *China National Space Administration* https://www.cnsa.gov.cn/n6758823/n6758838/c10355400/content.html (2023).
2. Niu, R. et al. Scientific objectives and suggestions on landing site selection of manned lunar exploration engineering. *Adv. Astronaut. Sci. Technol.* **7**, 37–50 (2024).
3. Hiesinger, H. et al. The Rima Bode region—candidate for a future lunar landing site. In *Proc. 52nd Lunar and Planetary Science Conference* abstr. 1485 (Lunar and Planetary Institute, 2021).
4. Milliken, R. E. & Li, S. Remote detection of widespread indigenous water in lunar pyroclastic deposits. *Nat. Geosci.* **10**, 561–565 (2017).
5. Gaddis, L. R. et al. Characterization and distribution of pyroclastic units in the Rima Bode region of the Moon. In *Proc. 12th Lunar and Planetary Science Conference* 318–320 (Lunar and Planetary Institute,1981).
6. Gaddis, L. R., Pieters, C. M. & Ray Hawke, B. Remote sensing of lunar pyroclastic mantling deposits. *Icarus* **61**, 461–489 (1985).
7. Hawke, B. R., Coombs, C. R., Gaddis, L. R., Lucey, P. G. & Owensby, P. D. Remote sensing and geologic studies of localized dark mantle deposits on the Moon. In *Proc. 19th Lunar and Planetary Science Conference* 255–268 (Lunar and Planetary Institute, 1989).
8. Pinori, S. & Bellucci, G. Imaging spectroscopy of selected regional dark mantle deposits of the Moon. *Planet. Space Sci.* **49**, 487–500 (2001).
9. Hagerty, J. J., Lawrence, D. J., Hawke, B. R. & Gaddis, L. R. New estimates of thorium abundances for the Rima bode pyroclastic glass deposit. In *Proc. 40th Lunar and Planetary Science Conference* abstr. 1852 (Lunar and Planetary Institute, 2009).
10. Gaddis, L. R. et al. Regional geology of lunar spinel-rich units in Sinus Aestuum. In *Proc. 45th Lunar and Planetary Science Conference* abstr. 2254 (Lunar and Planetary Institute, 2014).
11. Sunshine, J. M. et al. Hidden in plain sight: spinel-rich deposits on the nearside of the Moon as revealed by Moon Mineralogy Mapper (M3). In *Proc. 41st Lunar and Planetary Science Conference* abstr. 1508 (Lunar and Planetary Institute, 2010).
12. Weitz, C. M., Staid, M. I., Gaddis, L. R., Besse, S. & Sunshine, J. M. Investigation of lunar spinels at Sinus Aestuum. *J. Geophys. Res. Planets* **122**, 2013–2033 (2017).

13. Weitz, C. M., Head, J. W. & Pieters, C. M. Lunar regional dark mantle deposits: Geologic, multispectral, and modeling studies. *J. Geophys. Res. Planets* **103**, 22725–22759 (1998).
14. Heiken, G. H., McKay, D. S. & Brown, R. W. Lunar deposits of possible pyroclastic origin. *Geochim. Cosmochim. Acta* **38**, 1703–1718 (1974).
15. Pieters, C., McCord, T. B., Charette, M. P. & Adams, J. B. Lunar surface: identification of the dark mantling material in the Apollo 17 soil samples. *Science* **183**, 1191–1194 (1974).
16. Delano, J. W. & Livi, K. Lunar volcanic glasses and their constraints on mare petrogenesis. *Geochim. Cosmochim. Acta* **45**, 2137–2149 (1981).
17. Van Der Bogert, C. H. et al. Science-rich sites for in situ resource utilization characterization and end-to-end demonstration missions. *Planet. Sci. J.* **2**, 84 (2021).
18. Hiesinger, H. et al. Geology and absolute model ages of the Rima Bode region—a candidate future lunar landing site. In *Proc. 10th European Lunar Symposium (ELS 2022)* 25–26 (NASA Solar System Exploration Research Virtual Institute, 2022).
19. Lucey, P. G. et al. LEAG review of constellation program regions of interest for human exploration of the moon. In *Lunar Reconnaissance Orbiter Science Targeting Meeting* 73–74 (Lunar and Planetary Institute, Houston, 2009).
20. Clark, R. et al. Water and hydroxyl on the Moon as seen by the Moon Mineralogy Mapper (M3). In *Proc. 41st Lunar and Planetary Science Conference* abstr. 2302 (Lunar and Planetary Institute, 2010).
21. Li, S. & Milliken, R. E. Water on the surface of the Moon as seen by the Moon Mineralogy Mapper: distribution, abundance, and origins. *Sci. Adv.* **3**, e1701471 (2017).
22. Adams, J. B. in *Infrared and Raman Spectroscopy of Lunar and Terrestrial Minerals* (ed. Karr Jr, C.) 91–116 (Academic, 1975); https://doi.org/10.1016/B978-0-12-399950-4.50009-4.
23. Cloutis, E. A. & Gaffey, M. J. Spectral-compositional variations in the constituent minerals of mafic and ultramafic assemblages and remote sensing implications. *Earth Moon Planets* **53**, 11–53 (1991).
24. Cloutis, E. A. Pyroxene reflectance spectra: minor absorption bands and effects of elemental substitutions. *J. Geophys. Res. Planets* **107**, 6-1–6-12 (2002).
25. King, T. V. V. & Ridley, W. I. Relation of the spectroscopic reflectance of olivine to mineral chemistry and some remote sensing implications. *J. Geophys. Res. Solid Earth* **92**, 11457–11469 (1987).
26. Sunshine, J. M. & Pieters, C. M. Determining the composition of olivine from reflectance spectroscopy. *J. Geophys. Res. Planets* **103**, 13675–13688 (1998).
27. Martin, E. S. & Watters, T. R. Topography of nearside mare graben: implications for dike-induced or passive extension formation. *Icarus* **354**, 114039 (2021).
28. Hiesinger, H. et al. The Rima Bode region—absolute model ages of a candidate future lunar landing site. In *Proc. 53rd Lunar and Planetary Science Conference* Abstract 2169 (Lunar and Planetary Institute, 2022).
29. Barra, F. et al. ^{40}Ar/^{39}Ar dating of Apollo 12 regolith: implications for the age of Copernicus and the source of nonmare materials. *Geochim. Cosmochim. Acta* **70**, 6016–6031 (2006).
30. Papanastassiou, D. A. & Wasserburg, G. J. RbSr ages of igneous rocks from the Apollo 14 mission and the age of the Fra Mauro formation. *Earth Planet. Sci. Lett.* **12**, 36–48 (1971).
31. Deutsch, A. & Stöffler, D. Rb-Sr-analyses of Apollo 16 melt rocks and a new age estimate for the Imbrium basin: lunar basin chronology and the early heavy bombardment of the Moon. *Geochim. Cosmochim. Acta* **51**, 1951–1964 (1987).
32. Stadermann, F. J., Heusser, E., Jessberger, E. K., Lingner, S. & Stöffler, D. The case for a younger Imbrium basin: new ^{40}Ar-^{39}Ar ages of Apollo 14 rocks. *Geochim. Cosmochim. Acta* **55**, 2339–2349 (1991).
33. Snape, J. F. et al. Phosphate ages in Apollo 14 breccias: resolving multiple impact events with high precision U–Pb SIMS analyses. *Geochim. Cosmochim. Acta* **174**, 13–29 (2016).
34. Nemchin, A. A. et al. Ages of lunar impact breccias: limits for timing of the Imbrium impact. *Geochemistry* **81**, 125683 (2021).
35. Hiesinger, H. et al. How old are young lunar craters? *J. Geophys. Res.: Planets* **117**, 2011JE003935 (2012).
36. Iqbal, W., Hiesinger, H. & Van Der Bogert, C. H. Geological mapping and chronology of lunar landing sites: Apollo 12. *Icarus* **352**, 113991 (2020).
37. Mutch, T. A. *Geology of the Moon: A Stratigraphic View* (Princeton Univ. Press, 1973).
38. Gaddis, L. R., Staid, M. I., Tyburczy, J. A., Hawke, B. R. & Petro, N. E. Compositional analyses of lunar pyroclastic deposits. *Icarus* **161**, 262–280 (2003).
39. Xie, M., Liu, T. & Xu, A. Ballistic sedimentation of impact crater ejecta: implications for the provenance of lunar samples and the resurfacing effect of ejecta on the lunar surface. *J. Geophys. Res. Planets* **125**, e2019JE006113 (2020).
40. National Research Council *The Scientific Context for Exploration of the Moon* (National Academies Press, 2007).
41. McIntosh, E. C. et al. Revisiting the petrogenesis of pyroclastic glass bead deposits at the Apollo 15 and 17 sites. *J. Petrol.* **65**, egae026 (2024).
42. Delano, J. W. Apollo 15 green glass: chemistry and possible origin. In *Proc. 10th Lunar and Planetary Science Conference* 275–300 (Lunar and Planetary Institute, 1979).
43. Delano, J. W. Pristine lunar glasses: criteria, data, and implications. *J. Geophys. Res.: Solid Earth* **91**, 201–213 (1986).
44. Heiken, G. & McKay, D. Petrology of a sequence of pyroclastic rocks from the valley of Taurus-Littrow (Apollo 17 landing site). In *Proc. 9th Lunar and Planetary Science Conference* 1933–1943 (Lunar and Planetary Institute, 1978).
45. Jawin, E. R. et al. Lunar science for landed missions workshop findings report. *Earth Space Sci.* **6**, 2–40 (2019).
46. Gruener, J. E. & Joosten, B. K. NASA Constellation Program Office regions of interest on the Moon: A representative basis for scientific exploration, resource potential, and mission operations. In *Lunar Reconnaissance Orbiter Science Targeting Meeting* 50–51 (Lunar and Planetary Institute, Houston, 2009).
47. Sun, Z. et al. The technical design and achievements of Chang'E-3 probe. *Sci. Sin. Technol.* **44**, 331–343 (2014).
48. Jones, E. M. & Glover, K. Apollo lunar surface journal. *NASA* https://www.nasa.gov/history/alsj/ (2018).
49. Jones, E. M. Apollo 11 lunar surface journal. *NASA* https://apollojournals.org/alsj/a11/a11.html (2019).
50. Jones, E. M. Apollo 14 lunar surface journal. *NASA* https://apollojournals.org/alsj/a14/a14.html (2017).
51. Jones, E. M. Apollo 12 lunar surface journal. *NASA* https://apollojournals.org/alsj/a12/a12.html (2016).
52. Jones, E. M. Apollo 15 lunar surface journal. *NASA* https://apollojournals.org/alsj/a15/a15.html (2020).
53. Jones, E. M. Apollo 16 lunar surface journal. *NASA* https://apollojournals.org/alsj/a16/a16.html (2016).
54. Jones, E. M. Apollo 17 lunar surface journal. *NASA* https://apollojournals.org/alsj/a17/a17.html (2015).
55. Haase, I., Wählisch, M., Gläser, P., Oberst, J. & Robinson, M. S. Coordinates and maps of the Apollo 17 landing site. *Earth Space Sci.* **6**, 59–95 (2019).
56. Iqbal, W. et al. Slopes along Apollo EVAs: astronaut experience as input for future mission planning. *Acta Astronaut.* **223**, 184–196 (2024).
57. Haskin, L. A. The distribution of Th on the Moon's surface. In *Proc. 28th Lunar and Planetary Science Conference* abstr. 519 (Lunar and Planetary Institute, 1997).

58. Bates, J. R., Lauderdale, W. W. & Kernaghan, H. *ALSEP Termination Report* (NASA, 1979).
59. Nagihara, S. et al. Availability of previously lost data and metadata from the Apollo Lunar Surface Experiments Package (ALSEP). *Planet. Space Sci.* **191**, 105039 (2020).
60. Ping, J. et al. Lunar topographic model CLTM-s01 from Chang'E-1 laser altimeter. *Sci. China Ser. G* **52**, 1105–1114 (2009).
61. Robinson, M. S. et al. Lunar Reconnaissance Orbiter camera (LROC) instrument overview. *Space Sci. Rev.* **150**, 81–124 (2010).
62. Speyerer, E. J., Robinson, M. S., Denevi, B. W. & LROC Science Team Lunar Reconnaissance Orbiter camera global morphological map of the Moon. In *Proc. 42nd Lunar and Planetary Science Conference* abstr. 2387 (Lunar and Planetary Institute, 2011).
63. Kato, M., Takizawa, Y., Sasaki, S. & SELENE Project Team Selene, the Japanese lunar orbiting satellites mission: present status and science goals. In *Proc. 37th Lunar and Planetary Science Conference* abstr. 1233 (Lunar and Planetary Institute, 2006).
64. Barker, M. K. et al. A new lunar digital elevation model from the lunar orbiter laser altimeter and SELENE terrain camera. *Icarus* **273**, 346–355 (2016).
65. Cernan, E. A., Evans, R. E. & Schmitt, H. *Apollo 17 Technical Air-to-ground Voice Transcription*. Report No. MSC-07629 (NASA, 1972).
66. Lucchitta, B. K. Photogeology of the dark material in the Taurus-Littrow region of the Moon. In *Proc. 4th Lunar Science Conference* 149–162 (Pergamon Press, New York, 1973).
67. Lucchitta, B. K. & Schmitt, H. H. Orange material in the Sulpicius Gallus formation at the southwestern edge of Mare Serenitatis. In *Proc. 5th Lunar Science Conference* 223–234 (Pergamon Press, New York, 1974).
68. Carter, L. M., Campbell, B. A., Hawke, B. R., Campbell, D. B. & Nolan, M. C. Radar remote sensing of pyroclastic deposits in the southern Mare Serenitatis and Mare Vaporum regions of the Moon. *J. Geophys. Res. Planets* **114**, 2009JE003406 (2009).
69. Jawin, E. R. et al. The relationship between radar scattering and surface roughness of lunar volcanic features. *J. Geophys. Res. Planets* **119**, 2331–2348 (2014).
70. Campbell, B. A. et al. Earth-based 12.6-cm wavelength radar mapping of the Moon: new views of impact melt distribution and mare physical properties. *Icarus* **208**, 565–573 (2010).
71. Paige, D. A. et al. The Lunar Reconnaissance Orbiter Diviner lunar radiometer experiment. *Space Sci. Rev.* **150**, 125–160 (2010).
72. Bandfield, J. L. et al. Lunar surface rock abundance and regolith fines temperatures derived from LRO Diviner radiometer data. *J. Geophys. Res. Planets* https://doi.org/10.1029/2011JE003866 (2011).
73. Greenhagen, B. T. et al. Global silicate mineralogy of the Moon from the Diviner lunar radiometer. *Science* **329**, 1507–1509 (2010).
74. Hayne, P. O. et al. Global regolith thermophysical properties of the Moon from the Diviner lunar radiometer experiment. *J. Geophys. Res. Planets* **122**, 2371–2400 (2017).
75. Powell, T. M. et al. High-resolution nighttime temperature and rock abundance mapping of the Moon using the Diviner lunar radiometer experiment with a model for topographic removal. *J. Geophys. Res. Planets* **128**, e2022JE007532 (2023).
76. Williams, J. et al. Temperatures of the Lacus Mortis region of the Moon. *Earth Space Sci.* **9**, e2021EA001966 (2022).
77. Williams, J.-P. et al. Seasonal polar temperatures on the Moon. *J. Geophys. Res. Planets* **124**, 2505–2521 (2019).
78. Williams, J.-P., Paige, D. A., Greenhagen, B. T. & Sefton-Nash, E. The global surface temperatures of the Moon as measured by the Diviner lunar radiometer experiment. *Icarus* **283**, 300–325 (2017).
79. Powell, T. Replication data for: High-resolution nighttime temperature and rock abundance mapping of the Moon using the Diviner lunar radiometer experiment with a model for topographic removal. *UCLA Dataverse* https://doi.org/10.25346/S6/LFAVXU (2022).
80. Sato, H. et al. Lunar mare TiO_2 abundances estimated from UV/vis reflectance. *Icarus* **296**, 216–238 (2017).
81. Hapke, B., Sato, H. & Robinson, M. Lunar Reconnaissance Orbiter wide angle camera algorithm for TiO2 abundances on the lunar surface including low-Ti maria. *Icarus* **321**, 141–147 (2019); erratum **338**, 113544 (2020).
82. Hapke, B., Sato, H. & Robinson, M. Lunar Reconnaissance Orbiter wide angle camera algorithm for TiO_2 abundances on the lunar surface, including the highlands and low-Ti maria. *Icarus* **321**, 141–147 (2019).
83. Pieters, C. M. et al. The Moon Mineralogy Mapper (M^3) on Chandrayaan-1. *Curr. Sci.* **96**, 500–505 (2009).
84. Green, R. O. et al. The Moon Mineralogy Mapper (M^3) imaging spectrometer for lunar science: instrument description, calibration, on-orbit measurements, science data calibration and on-orbit validation. *J. Geophys. Res.* **116**, E00G19 (2011).
85. Boardman, J. W. et al. Measuring moonlight: an overview of the spatial properties, lunar coverage, selenolocation, and related level 1B products of the Moon Mineralogy Mapper. *J. Geophys. Res.* **116**, E00G14 (2011).
86. Clark, R. N., Pieters, C. M., Green, R. O., Boardman, J. W. & Petro, N. E. Thermal removal from near-infrared imaging spectroscopy data of the Moon. *J. Geophys. Res.* **116**, E00G16 (2011).
87. Besse, S. et al. Deriving a photometric model for the Moon Mineralogy Mapper data (M3). In *Proc. 42nd Lunar and Planetary Science Conference* abstr. 1773 (Lunar and Planetary Institute, 2011).
88. Hicks, M. D. et al. A photometric function for analysis of lunar images in the visual and infrared based on Moon Mineralogy Mapper observations. *J. Geophys. Res.* **116**, E00G15 (2011).
89. Isaacson, P. J. et al. Development, importance, and effect of a ground truth correction for the Moon Mineralogy Mapper reflectance data set. *J. Geophys. Res. Planets* **118**, 369–381 (2013).
90. Isaacson, P., Besse, S. & Nettles, J. *M^3 Overview and Working with M^3 Data* (NASA, 2011); https://pds-imaging.jpl.nasa.gov/documentation/Isaacson_M3_Workshop_Final.pdf
91. Horgan, B. H. N., Cloutis, E. A., Mann, P. & Bell, J. F. Near-infrared spectra of ferrous mineral mixtures and methods for their identification in planetary surface spectra. *Icarus* **234**, 132–154 (2014).
92. Henderson, M. J. B., Horgan, B. H. N., Lawrence, S. J., Stopar, J. D. & Gaddis, L. R. Mineralogy of explosive and effusive volcanic edifices in the Marius Hills volcanic complex. *Icarus* **404**, 115628 (2023).
93. Quaide, W. L. & Oberbeck, V. R. Thickness determinations of the lunar surface layer from lunar impact craters. *J. Geophys. Res.* **73**, 5247–5270 (1968).
94. Fa, W., Liu, T., Zhu, M.-H. & Haruyama, J. Regolith thickness over Sinus Iridum: results from morphology and size–frequency distribution of small impact craters. *J. Geophys. Res. Planets* **119**, 1914–1935 (2014).
95. Bart, G. D., Nickerson, R. D., Lawder, M. T. & Melosh, H. J. Global survey of lunar regolith depths from LROC images. *Icarus* **215**, 485–490 (2011).
96. Xie, M., Xiao, Z., Zhang, X. & Xu, A. The provenance of regolith at the Chang'e-5 candidate landing region. *J. Geophys. Res. Planets* **125**, e2019JE006112 (2020).
97. Baldwin, R. B. Relative and absolute ages of individual craters and the rate of infalls on the Moon in the post-Imbrium period. *Icarus* **61**, 63–91 (1985).

98. Neukum, G., König, B. & Arkani-Hamed, J. A study of lunar impact crater size-distributions. *Moon* **12**, 201–229 (1975).
99. Neukum, G. & Ivanov, B. A. Crater size distributions and impact probabilities on Earth from lunar, terrestrial-planet, and asteroid cratering data. *Hazards Due Comets Asteroids* **359**, 359–416 (1994).
100. Hiesinger, H., Jaumann, R., Neukum, G. & Head, J. W. Ages of mare basalts on the lunar nearside. *J. Geophys. Res. Planets* **105**, 29239–29275 (2000).
101. Neukum, G., Ivanov, B. A. & Hartmann, W. K. Cratering records in the inner solar system in relation to the lunar reference system. *Space Sci. Rev.* **96**, 55–86 (2001).
102. Heyer, T. et al. A comparative analysis of global lunar crater catalogs using OpenCraterTool—An open source tool to determine and compare crater size-frequency measurements. *Planet. Space Sci.* **231**, 105687 (2023).
103. McEwen, A. S. & Bierhaus, E. B. The importance of secondary cratering to age constraints on planetary surfaces. *Annu. Rev. Earth Planet. Sci.* **34**, 535–567 (2006).
104. Michael, G. G. & Neukum, G. Planetary surface dating from crater size–frequency distribution measurements: partial resurfacing events and statistical age uncertainty. *Earth Planet. Sci. Lett.* **294**, 223–229 (2010).
105. Neukum, G. *Meteorite Bombardment and Dating of Planetary Surfaces*. Habilitation thesis, Univ. Munich (1983).
106. Michael, G. G., Kneissl, T. & Neesemann, A. Planetary surface dating from crater size-frequency distribution measurements: Poisson timing analysis. *Icarus* **277**, 279–285 (2016).
107. Michael, G. G., Platz, T., Kneissl, T. & Schmedemann, N. Planetary surface dating from crater size–frequency distribution measurements: spatial randomness and clustering. *Icarus* **218**, 169–177 (2012).
108. Malaret, E. et al. CH1-ORB MOON M3 4 L2 REFLECTANCE NEAR-IR SPECTRAL IMGS V1.0. *NASA Planetary Data System* https://doi.org/10.17189/1520414 (2011).
109. Yang, M. 'Geology of Rimae Bode region as priority site candidate for China's first crewed lunar mission' dataset. *Zenodo* http://zenodo.org/records/17767133 (2025).
110. Wilhelms, D. E. *The Geologic History of the Moon*. Professional Paper 1348 (*USGS*, 1987).
111. Li, C. et al. Laser altimetry data of Chang'E-1 and the global lunar DEM model. *Sci. China Earth Sci.* **53**, 1582–1593 (2010).

Acknowledgements

We acknowledge the use of imagery from Lunar QuickMap (https://lunar.quickmap.io), a collaboration between NASA, Arizona State University and Applied Coherent Technology Corp. S.H. was funded by the National Natural Science Foundation of China (Grant No. 42241104). J.H. was funded by the M-0016 Sino-German mobility project granted by the Sino-German Science Center of the National Natural Science Foundation of China. L.X. was funded by the Science and Technology Development Fund of Macau (Grant No. 0052/2024/RIA1). M.X. was funded by the National Natural Science Foundation of China (Grant No. 12173011).

Author contributions

J.H. designed the research. M.Y. processed the remote-sensing data. M.Y., W.I., L.W. and S.M. conducted the CSFD study. M.X. produced the ballistic sedimentation model. M.Y. and J.H. analysed and interpreted the results with input from W.I., L.W. and S.M. M.Y., J.H., W.I., L.W., C.H.v.d.B. and H.H. wrote the paper. M.Y. produced the figures. All authors reviewed the paper.

Competing interests

The authors declare no competing interests.

Additional information

Extended data is available for this paper at https://doi.org/10.1038/s41550-026-02790-0.

Supplementary information The online version contains supplementary material available at https://doi.org/10.1038/s41550-026-02790-0.

Correspondence and requests for materials should be addressed to Jun Huang.

Peer review information *Nature Astronomy* thanks Edward Cloutis and Noah Petro for their contribution to the peer review of this work.

Reprints and permissions information is available at www.nature.com/reprints.

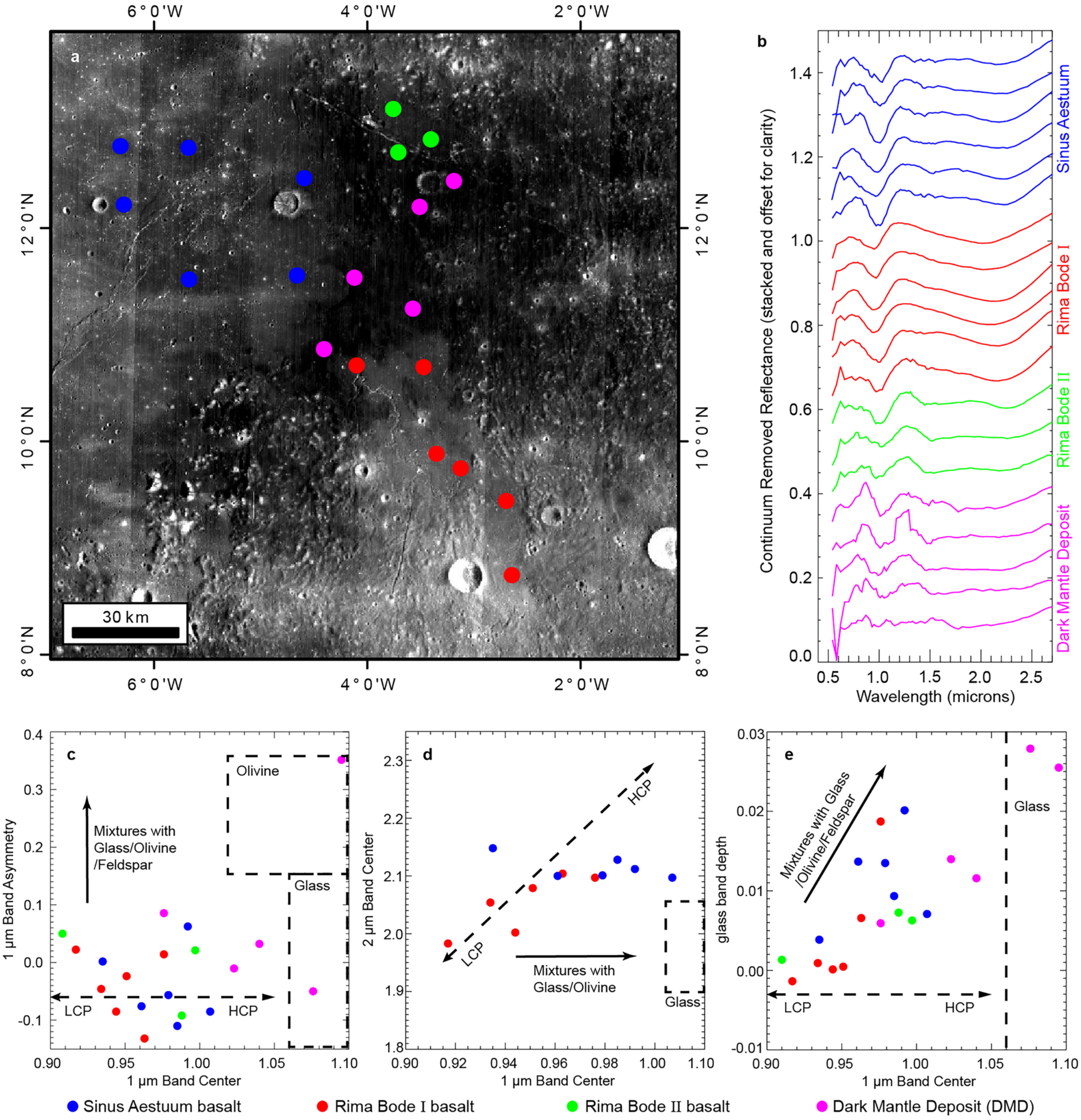

Extended Data Fig. 1 | Spectral characteristics of the Rimae Bode region from M3 data. (**a**) Locations of points of interest within each geological unit used for spectral analysis, shown on the M^3 750 nm reflectance mosaic. (**b**) Continuum-removed reflectance spectra. (**c**-**e**) Band-parameter plots used to identify the dominant spectral components: (**c**) 1 µm band center (B1cen) vs. 1 µm band asymmetry (B1asy); (**d**) 1 µm band center vs. 2 µm band center (B2cen). (**e**) 1 µm band center vs. glass band depth. Dashed lines and boxes outline the characteristic parameter ranges for each material after Horgan et al.[91].

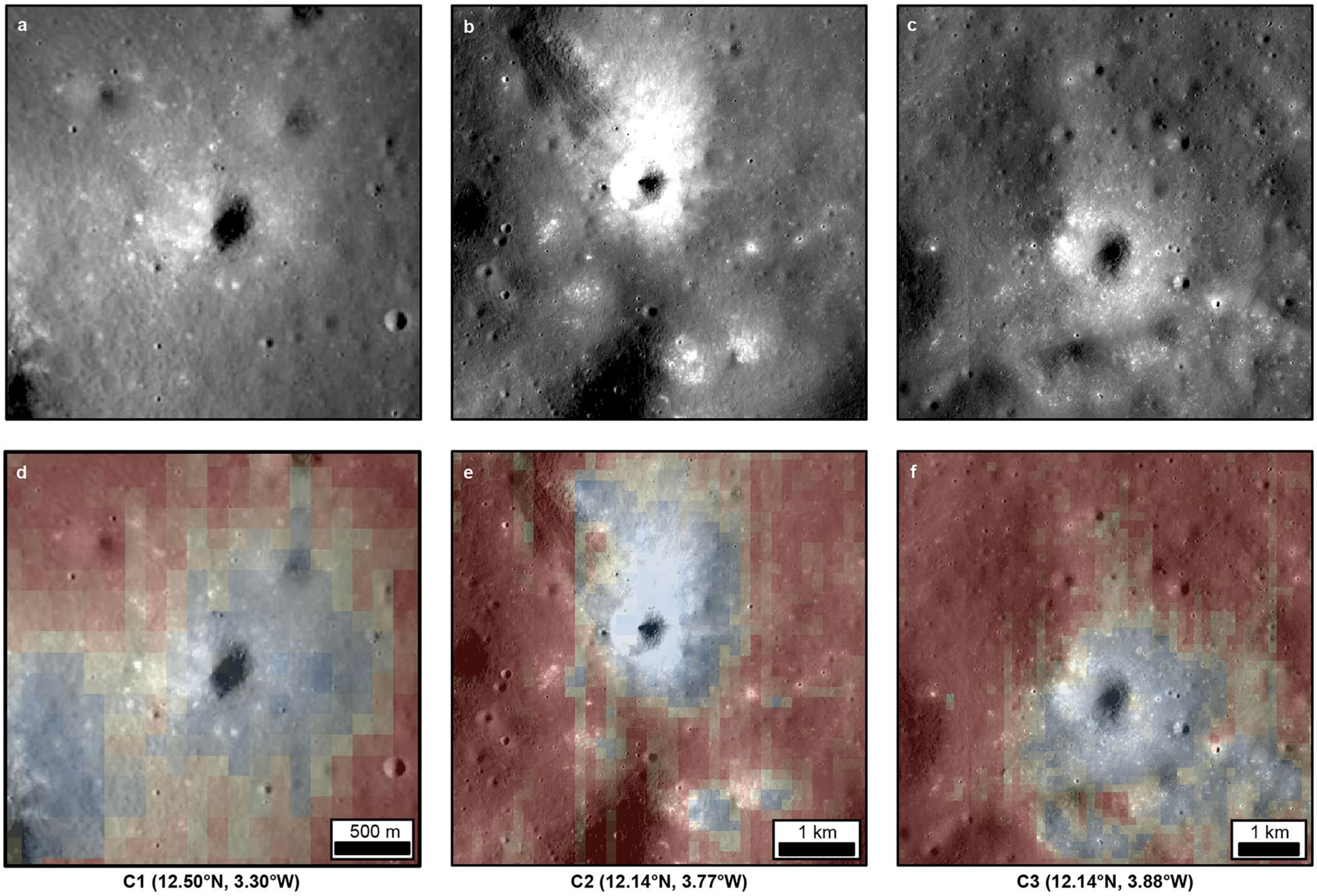

Extended Data Fig. 2 | Three impact craters that penetrate the DMD unit. (**a**-**c**) Kaguya TC morning map of the three craters. (**d**-**f**) Glass band depth values draped over the same TC mosaics. Detailed information on the three impact craters is shown in the Supplementary Table 1.

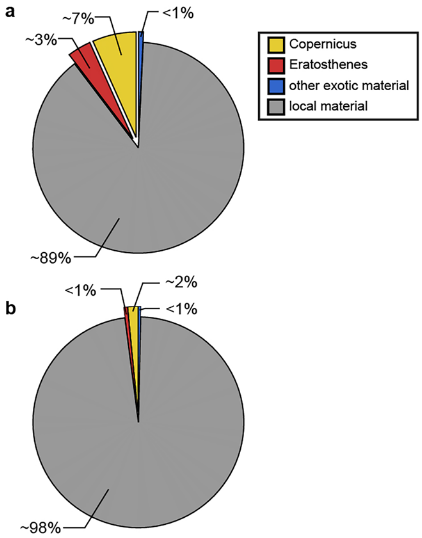

Extended Data Fig. 3 | Estimated ejecta abundance by ballistic sedimentation model. (**a**) Modeled surface contributions of local and exotic materials at proposed landing site 1 (red star in Fig. 1). (**b**) Same as (**a**) but at a depth of 10 m. Chart segments show mass percentages of local material (grey), Copernicus ejecta (yellow), Eratosthenes ejecta (red), and other exotic ejecta (blue), including contributions from Pythagoras, Reinhold, Theophilus and Aristillus.

https://doi.org/10.1038/s41550-026-02790-0

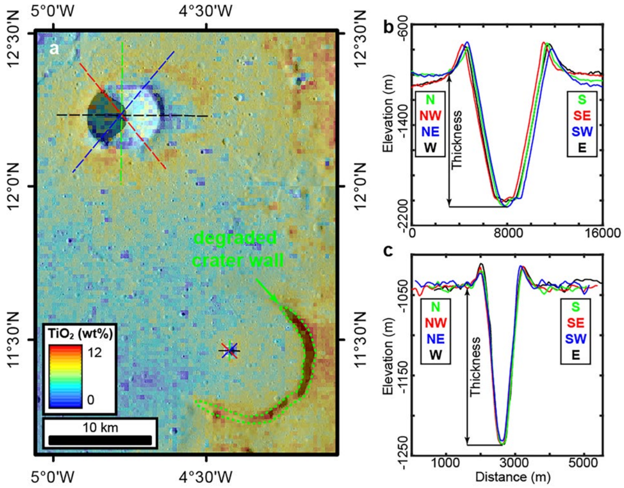

Extended Data Fig. 4 | Two craters that penetrated the Sinus Aestuum basalt. (**a**) WAC TiO_2 abundance map overlain on the Kaguya TC morning map. Coloured dashed lines mark profile locations in four directions: green (N–S), red (NW–SE), blue (NE–SW) and black (E–W). (**b**, **c**) Topographic profiles in four directions across Bode C (**b**) and a fresh small crater (**c**). The elevation difference between the flat terrain outside the rim and the crater floor is taken as the maximum thickness of the Sinus Aestuum basalt.

https://doi.org/10.1038/s41550-026-02790-0

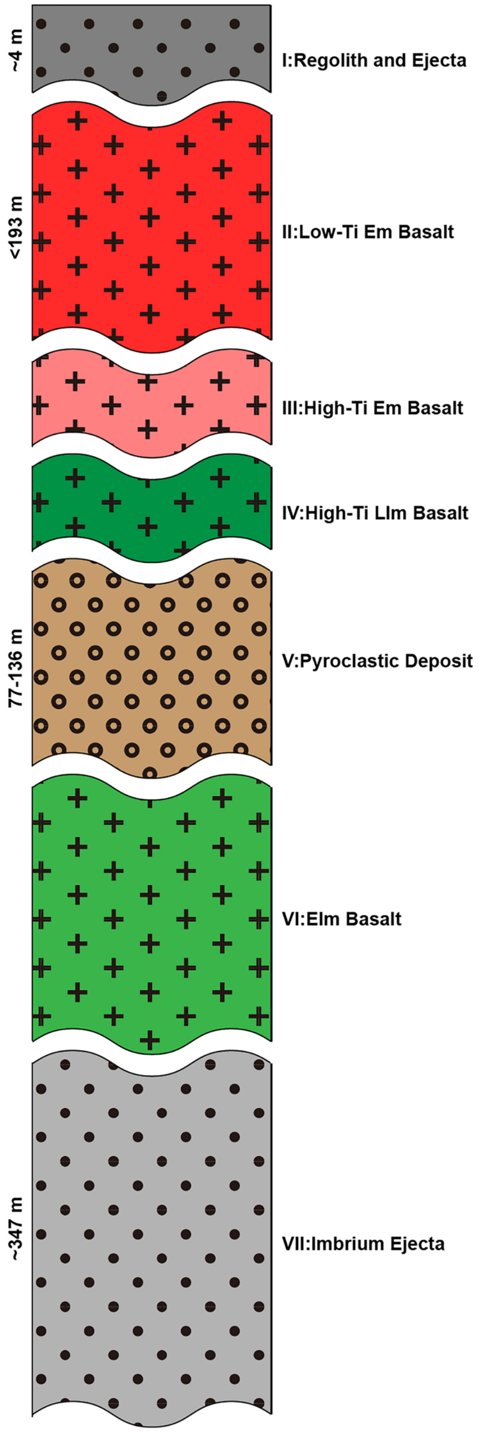

Extended Data Fig. 5 | Conceptual geological column at the proposed landing site 1. The location is indicated by the red star in Fig. 1.

Extended Data Table 1 | Craters used in the Ballistic Sedimentation Model to analyze exotic ejecta thicknesses

Crater Name	Lat (°)	Lon (°)	Ejecta Thickness (m)	Age
Copernicus	9.62	-20.08	0.30	779 Ma[a]; 782 Ma[b]; 796 Ma[c]
Aristillus	33.88	1.21	0.01	1.83 Ga[d]
Theophilus	-11.45	26.28	0.02	2.03 Ga[d]
Pythagoras	63.68	-62.98	0.02	2.68 Ga[e]
Reinhold	3.28	-22.86	0.01	2.82 Ga[d]
Eratosthenes	14.47	-11.32	0.57	2.97 Ga[d]

[a]Hiesinger et al.[35], [b]Barra et al.[29], [c]Iqbal et al.[36], [d]Baldwin et al.[97], [e]Xie et al.[96]

Extended Data Table 2 | Science concepts and goals in Rimae Bode region based on the NRC report[40]

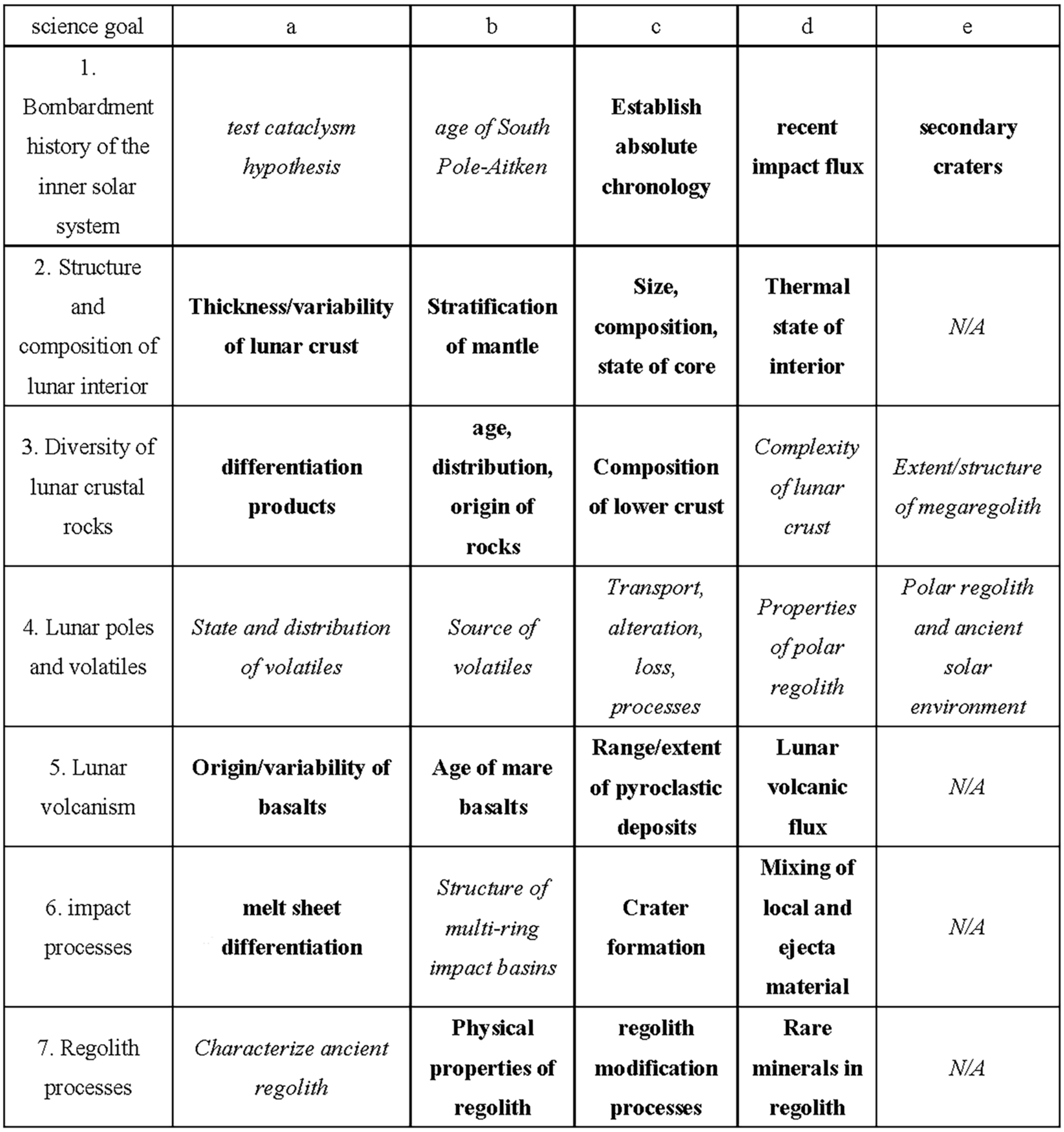

science goal	a	b	c	d	e
1. Bombardment history of the inner solar system	*test cataclysm hypothesis*	*age of South Pole-Aitken*	**Establish absolute chronology**	**recent impact flux**	**secondary craters**
2. Structure and composition of lunar interior	**Thickness/variability of lunar crust**	**Stratification of mantle**	**Size, composition, state of core**	**Thermal state of interior**	*N/A*
3. Diversity of lunar crustal rocks	**differentiation products**	**age, distribution, origin of rocks**	**Composition of lower crust**	*Complexity of lunar crust*	*Extent/structure of megaregolith*
4. Lunar poles and volatiles	*State and distribution of volatiles*	*Source of volatiles*	*Transport, alteration, loss, processes*	*Properties of polar regolith*	*Polar regolith and ancient solar environment*
5. Lunar volcanism	**Origin/variability of basalts**	**Age of mare basalts**	**Range/extent of pyroclastic deposits**	**Lunar volcanic flux**	*N/A*
6. impact processes	**melt sheet differentiation**	*Structure of multi-ring impact basins*	**Crater formation**	**Mixing of local and ejecta material**	*N/A*
7. Regolith processes	*Characterize ancient regolith*	**Physical properties of regolith**	**regolith modification processes**	**Rare minerals in regolith**	*N/A*

Bold entries denote science goals that can be addressed; italic entries denote goals that cannot be addressed.

Extended Data Table 3 | The travers ability conditions (Fig. 5) and scientific objectives of the Rimae Bode region

Engineering conditions	Scientific objectives
1. lunar nearside (direct data transmission)	1. pyroclastic deposits
2. low latitude (extensive solar power)	2. volcanic structures
3. relatively flat terrain (slope $< 8^\circ$, safe landing)[53]	3. high-thorium material
	4. Copernicus and Eratosthenes ejecta

Extended Data Table 4 | Proposed landing sites and the characteristics of potential returned samples

Landing site	Lat (°)	Lon (°)	Samples types	science goals[a]
LS1	11.70	-4.40	1. Sinus Aestuum basalts	1c, 3b, 5a, 6d, and 7b-c
			2. pyroclastics	5c-d
			3. high-Ti ejecta	5c, and 6c-d
			4. Copernicus ray	1c, 3a, and 7c
LS2	12.68	-3.74	1. high-Th basalt	1c, 2d, 3a-b, 5a, and 7b-c
			2. pyroclastics	5c-d
			3. Rima Bode II	3b, 5a, and 5d
			4. Imbrium ejecta	1c, 3a, and 7c
LS3	12.27	-4.35	1. Sinus Aestuum basalts	1c, 3b, 5a, 6c, and 7b-c
			2. pyroclastics	5c-d
			3. Bode C ejecta	5c, and 6c-d
LS4	10.70	-4.06	1. low-Ti basalt	1c, 3b, 5a, 6d, and 7b-c
			2. pyroclastics	5c-d
			3. Rima Bode I	3b, and 5a

[a] National Research Council et al.[46]

Landing site names correspond to their designations in Fig. 5.